Mechanical Systems and Signal Processing 173 (2022) 109063

Contents lists available at ScienceDirect

Mechanical Systems and Signal Processing

journal homepage: www.elsevier.com/locate/ymssp

A novel long-stroke fast tool servo system with counterbalance and its application to the ultra-precision machining of microstructured surfaces

Zheng Gong [a], Dehong Huo [a,*], Zengyuan Niu [b], Wanqun Chen [c], Kai Cheng [d]

[a] School of Engineering, Newcastle University, Newcastle upon Tyne NE1 7RU, UK
[b] Uptech, Jiangsu Industrial Technology Research Institute, Kunshan, Jiangsu Province 215300, China
[c] School of Electromechanical Engineering, Soochow University, Soochow 215031, China
[d] School of Engineering and Design, Brunel University London, UB8 3PH, UK

ARTICLE INFO

Communicated by John E. Mottershead

Keywords:
Fast tool servo
Hybrid control algorithm
Counterbalance
System vibration
Microstructured surface

ABSTRACT

This paper presents a novel long-stroke fast tool servo (FTS) system with counterbalance and its application to the diamond machining of microstructured surfaces. The FTS system is driven by a voice coil motor and guided by air bearings. A hybrid control algorithm which combines PID control, sliding mode control and feed-forward control was specifically designed for the system and ensures that it has less than 1% tracking error and achieves ± 1 mm stroke and 105 Hz bandwidth. The counterbalance is achieved by the symmetric arrangement of two of the same FTS systems. System vibration decreased significantly from ± 3 μm to ± 0.145 μm when the counterbalance was working. Machining experiments were conducted using the FTS system on a diamond turning machine. A microstructured surface simulation model was built and information about the workpiece surface tested and collected. When the counterbalance was working, error in the machine axes decreased from micron-level to nano-level and the surface roughness of the microstructured surface was also reduced. The system achieves ± 1 mm (±0.5 mm) stroke at 30 Hz (40 Hz) with 0.35% (0.68%) tracking error during machining processes, and the depth error of the machined microstructured surface was measured at 1.4% (2.3%).

1. Introduction

Fast tool servo (FTS) in diamond turning is an effective technique for machining high precision components like asymmetric optical surfaces or microarrays [1]. According to the main driving source, Trumper et al. [2] introduced five different FTS systems: hydraulic, piezoelectric, magnetostrictive, Lorentz force, and normal-stress electromagnetically-driven FTS. Among these, piezoelectric FTS (PZT-FTS) and Lorentz force FTS (LF-FTS) are most widely used. Gan et al. [3] combined a force monitoring system with the PZT-FTS. The FTS system had a 15 μm stroke and 2 kHz bandwidth and the system was effective especially in machining waveform profiles with small cutting depth. Ma et al. [4] developed a flexure hinge to give the PZT-FTS the ability to track a ± 400 μm sinusoidal signal at 100 Hz. Precitech Inc [5] developed PZT-FTS 70/35, which can travel at 70/35 μm stroke with a maximum operating frequency of 0.9/1 kHz. It can be used on the machining of microlenses on a brass disk. Wang et al. [6] designed a PZT-FTS with motion amplification,

* Corresponding author.
E-mail address: dehong.huo@newcastle.ac.uk (D. Huo).

https://doi.org/10.1016/j.ymssp.2022.109063
Received 8 November 2021; Received in revised form 24 January 2022; Accepted 17 March 2022
Available online 26 March 2022

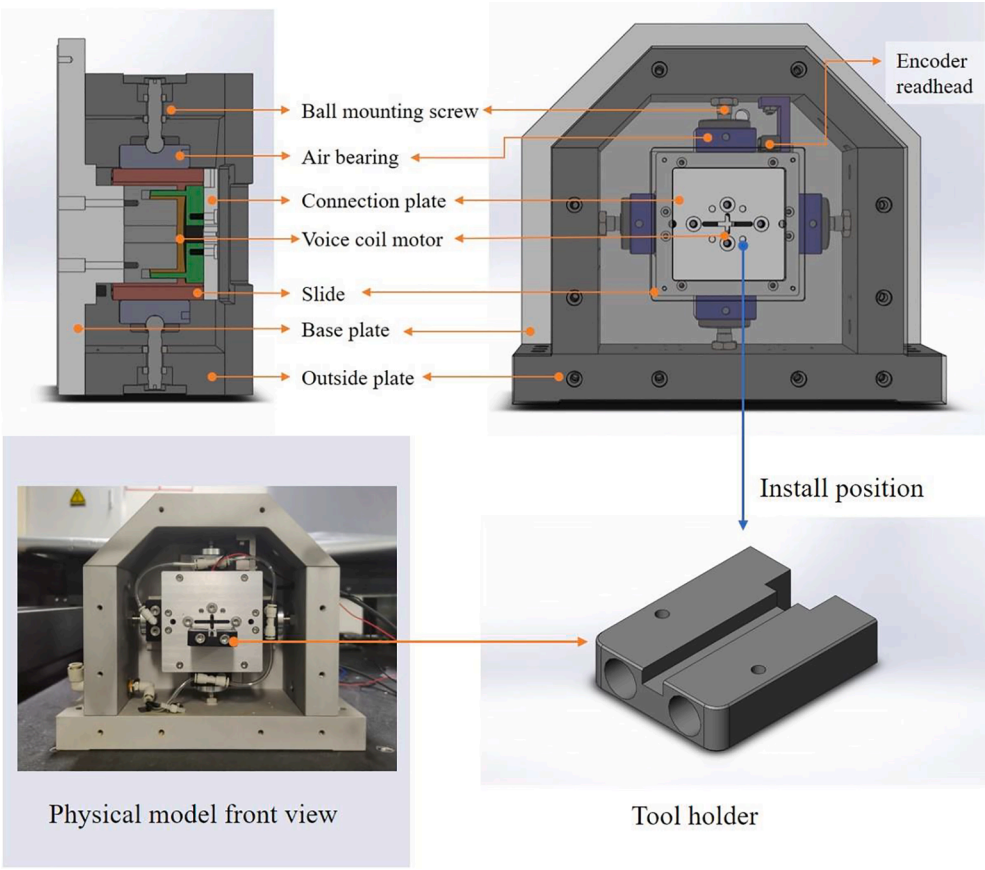

Fig. 1. Mechanical structure of design FTS.

which can be used for the noncircular piston turning process. The system owned 540 μm to 0.3 mm stroke and 321 Hz resonant frequency. Thomas et al. [7] used a voice coil motor (VCM), a hollow triangle slide and air bearings to achieve 4 mm travel and 2.5 mm/s maximum tool speed. It was designed to manufacture biconic mirrors and the RMS shape error was 0.7 μm. Marten [8] developed a long-stroke FTS which includes an air bearing stage and a three-phase oil-cooled linear motor. The system can achieve 25 mm stroke and 100 g acceleration. Feng et al. [9] designed an LF-FTS with a VCM and a slide to fabricate freeform lenses. The PI and feedforward controllers helped the system achieve a 1.5 mm stroke at 16.67 Hz. Another LF-FTS with similar functions was designed by Liu et al. [10], the system was built by a VCM and a flexure hinge. The achieved performance was a 1 mm stroke at 30 Hz. Precitech Inc [11] developed FTS 5000, which consists of a voice coil motor and air bearings. It can travel 5 mm and the servo bandwidth was more than 1 kHz. Some typical operational sinusoidal accelerations were given, such as 2000 μm at 100 Hz and 100 μm at 440 Hz. Overall, to achieve high frequency, the piezoelectric ceramic was combined with a flexure hinge. To achieve a long stroke, the combination of a linear motor and air bearings is the better choice.

The control algorithm is also important for system performance. Wu et al. [12] proposed a control algorithm combining machine learning and PID feedback control, and the system achieved 0.54% average linearity. Zhou et al. [13] used adaptive feed-forward control (AFC) and neural network control to compensate for the hysteresis of the PZT ceramics, and simulation results showed that the PZT FTS was robust in tracking the input signal with frequency variations. Dan Wu et al. [14] adopted active disturbance rejection control (ADRC) and an extended state observer to control an FTS system driven by VCM, and the RMS tracking error was approximately 1.6–1.7 μm. Zhang et al. [15] presented a sliding mode controller for a PZT-FTS. With the help of the combined approaching law, the following error of the sinusoidal signal was 0.57%. Also, sliding mode control can work with repetitive and feedforward control [16]. The PZT-FTS system tracking error with this novel controller was decreased from 10.92% to 0.82% compared to the system with the PID control. Zero-phase error tracking control (ZPETC) [17], genetic algorithm, fuzzy control were also options for the FTS system control algorithms. Specifically, fuzzy and PID control helped a feed servo system achieve online auto-tuning [18], and double-feedforward compensation can effectively decrease phase error [19]. Furthermore, the FTS system control algorithm was always formed by two or three different control methods. The combinations of different control methods are worthy of further study. Most research has focused on PZT-FTS control algorithms, but fewer studies have been carried on the control algorithms of LF-FTS. Even though control algorithms for linear motors are well-developed, the combination of the motor and air bearings in FTS applications mean that the system becomes undamped. An appropriate control algorithm and potential problems for the LF-FTS control

Fig. 2. Seven-orifice air bearing pad.

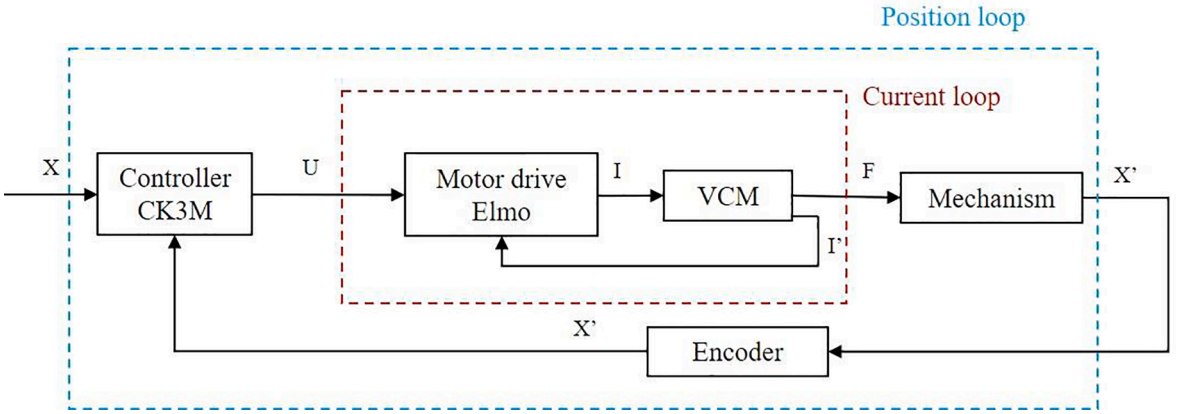

Fig. 3. Control system structure of designed FTS.

system require research attention.

Counterbalance has been designed and discussed in some studies. Chen et al. [20] designed an FTS system (FLORA) without counterbalance, and the dynamic conditions greatly affected the quality of surface finish and form error. Based on FLORA, Erik [21] used two small motors and well-designed springs to achieve counterbalance. Marten and David et al. [22] described a linear long-stroke FTS system with integral balance mass. The mass moved freely in response to the FTS motor force. Liu et al. [23] introduced three ways to achieve counterbalance using flexible components, the symmetrical arrangement of two of the same FTS systems and using an infeed slideway or reaction mass. Counterbalance is beneficial for the FTS system and the whole machining system but details of its effects, including how it decreases system vibration and affects the surface quality of a workpiece, have not been considered.

In this paper, a novel LF-FTS system is developed based on the voice coil motor and air bearings. Counterbalance is achieved by the back-to-back connection of two of the same FTS systems. A hybrid control algorithm is developed according to the system control model. Performance tests including step response, sinusoidal signal tracking tests and bandwidth tests, were applied to evaluate the FTS system's performance. The performance of the counterbalance and its effect was simulated in Ansys and tested by a laser displacement sensor. Finally, the FTS system was installed on a diamond turning machine and four workpieces were machined and tested. A microstructured surface simulation model was also built according to the experimental parameters. Microstructured surface depth, overcut depth and surface roughness were measured and compared.

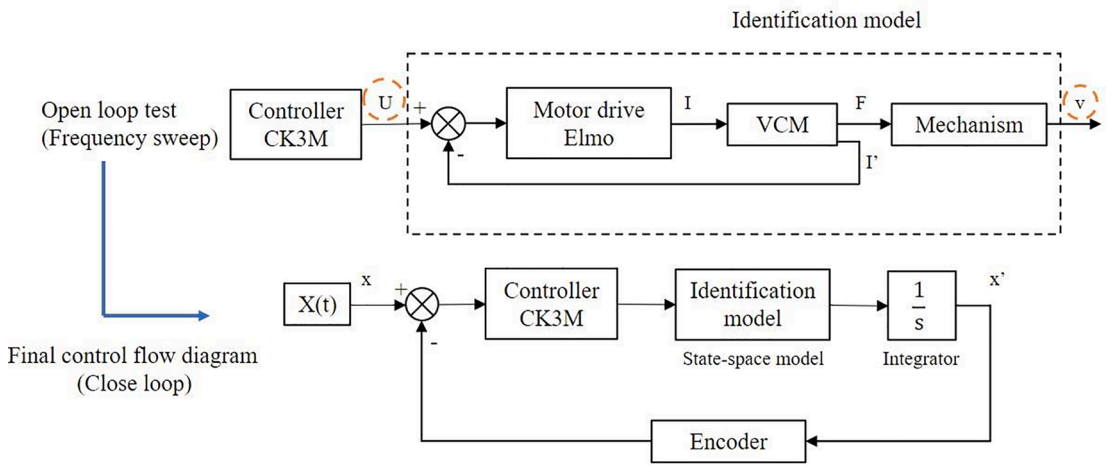

Fig. 4. System identification processes.

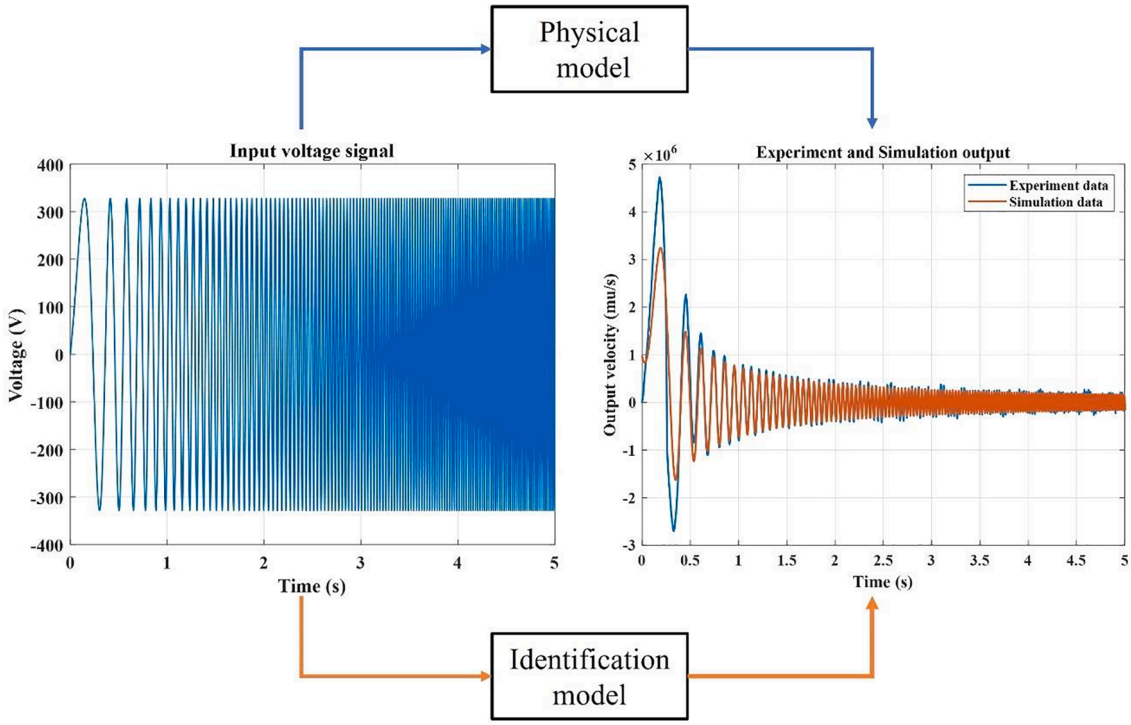

Fig. 5. Comparison of the physical model output and identification model output.

2. Design of the fast tool servo system

2.1. Overview of the FTS design

As illustrated in Fig. 1, the designed FTS system consists of a square hollow slide driven by a voice coil motor and supported by four air bearings. The air bearings are attached to the outside plate by ball mounting screws and high-resolution optical encoders are also installed on the outside plate to provide feedback displacement signals. The tool holder is installed on the connection plate and it is ensured that the tool motion is coaxial with the motor motion. The designed FTS has a stroke of ± 1.5 mm, a maximum working frequency of 100 Hz and a motor force of 64.6 N. The seven-orifice air bearing (see Fig. 2) withs a stiffness of 31.05 N/μm is installed with 10 μm air film height.

The controller is the CK3M from Omron which runs the position loop, while the current loop is achieved by the Elmo motor drive.

Table 1
Control parameters and functions.

Parameters	Functions	Value
K_p	Proportional gain	5.813
K_i	Integration gain	0.00125
K_d	Differentiation gain	0.005625
K_1	Sliding surface parameters (stiffness)	12
K_2	Sliding surface parameters (damping)	0.08
K_3	Control law parameters	0.2
K_4	Control law parameters	0.1
K_{vff}	Velocity feedforward gain	0.5
K_{aff}	Acceleration feedforward gain	1600

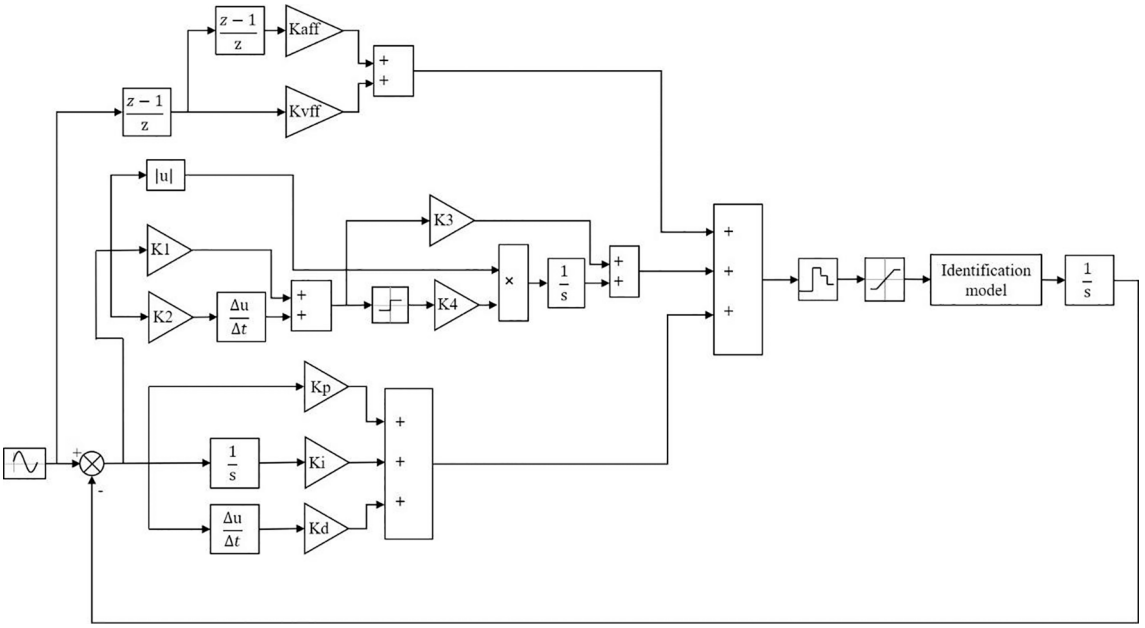

Fig. 6. Simulation model of the designed FTS system.

Position feedback is achieved by the Renishaw encoder which is attached to the slide. The control system structure is shown in Fig. 3.

2.2. System identification

The control model of the designed system can be identified from an open loop frequency sweep. A frequency varying voltage signal is generated from the controller and drives the designed system. The stroke of the system is recorded by the encoder and automatically transformed to a velocity signal. The system control parameters are calculated from the output velocity and input voltage. In addition, the voltage signal and displacement signal in the controller are in the form of a digital signal. Transformation from digital to analogue signals are needed: the output voltage of the controller is a ± 10 V analogue signal corresponding to a ± 32768 digital signal; the encoder transforms the 10 nm displacement signal into a 1 mu digital signal. After the open loop identification model is determined and combined with the control system structure, the final control flow diagram of the designed FTS can be drawn and used for further control algorithm developments. The system identification processes are shown in Fig. 4.

The state-space model is adopted to fit the experiment data, as shown in Eq. (1).

$$\begin{cases} dx/dt = Ax(t) + Bu(t) + Ke(t) \\ y(t) = Cx(t) + Du(t) + e(t) \end{cases} \tag{1}$$

In the equation:

$A = -11.37$, $B = 0.0006759$, $C = 2.293 \times 10^8$, $D = 0$, $K = 3.877 \times 10^{-5}$;

K is a small number and $e(t)$ represents disturbances in the system, and A, B, C, D are the constants. In this research, the identification model neglects disturbances. A comparison between the physical model and identification model outputs is shown in Fig. 5. It can be seen that the amplitude difference occurs in the first three periods and no obvious phase difference is observed. This means that the system identification model can be used to represent the physical model to a certain extent, and hence it has been used to adjust the

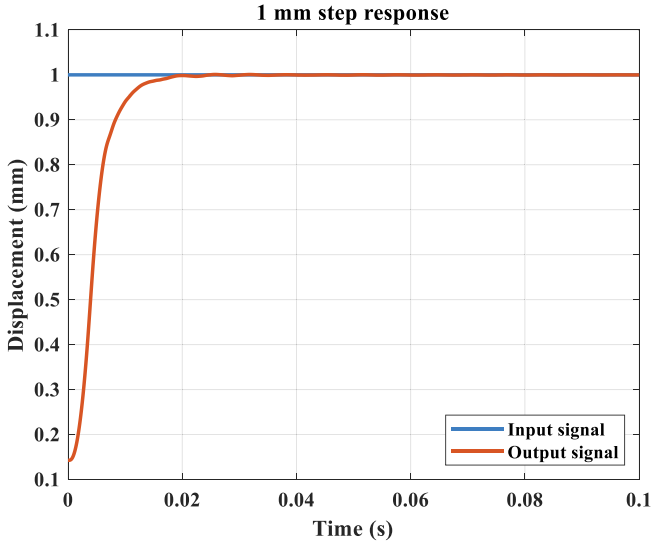

Fig. 7. 1 mm step response.

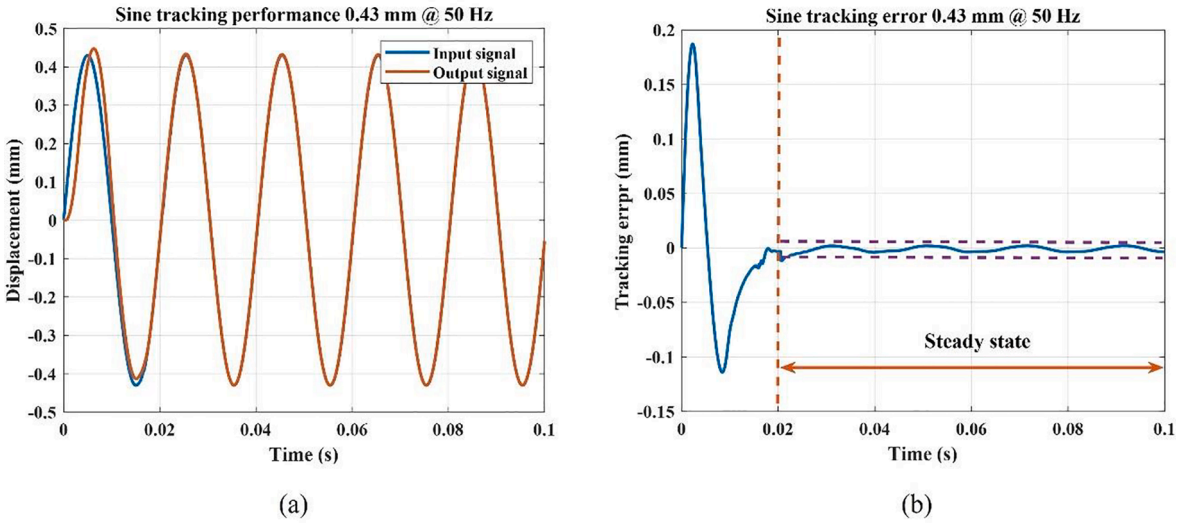

Fig. 8. Sine tracking performance and error (0.43 mm @ 50 Hz).

control parameters in advance for the physical model.

2.3. Hybrid control algorithm

A hybrid control algorithm was designed for the FTS system [24]. The control algorithm is a combination of PID control, sliding mode control (SMC) and feed-forward (FF) control. The control output is described in Eq. (5):

$$c(t)_{PID} = K_p e(t) + K_i \int_o^t e(t)dt + K_d \frac{de(t)}{dt} \tag{2}$$

$$\begin{cases} S = K_1 e(t) + K_2(e(t) - e(t-1)) \\ c(t)_{SMC} = K_3 S + \int_0^t (K_4 \bullet \quad sign(S) \bullet |e(t)|)dt \end{cases} \tag{3}$$

$$c(t)_{FF} = K_{vff} \frac{dx(t)}{dt} + K_{aff} \frac{d^2x(t)}{dt^2} \tag{4}$$

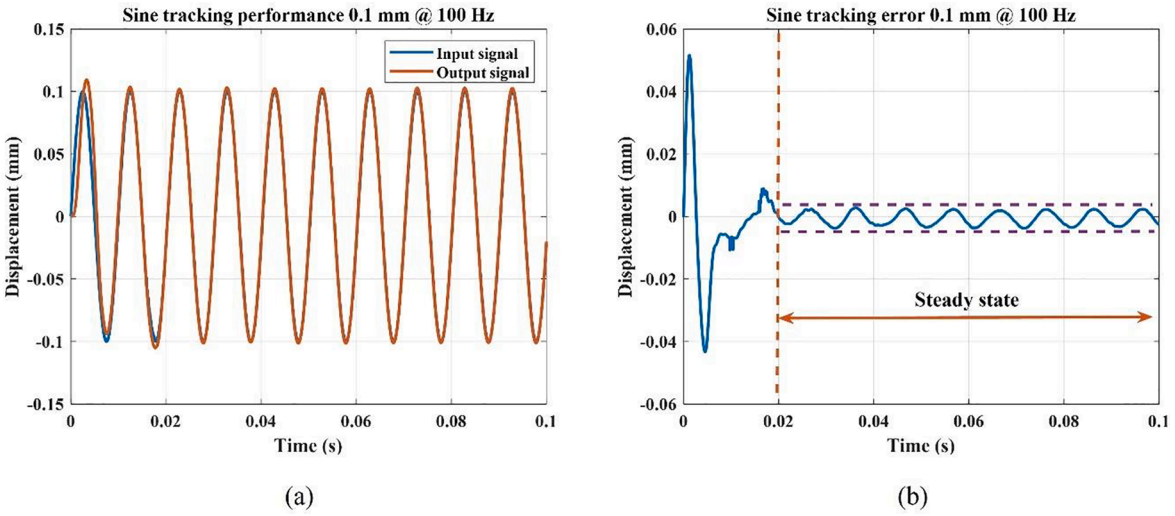

Fig. 9. Sine tracking performance and error (0.1 mm @ 100 Hz).

Table 2
Steady-state error of the designed system.

Steady-state error (mm & %)				
30 Hz (1 mm)	40 Hz (0.68 mm)	50 Hz (0.43 mm)	60 Hz (0.3 mm)	100 Hz (0.1 mm)
0.00364	0.0040392	0.0037453	0.004005	0.00374
0.364%	0.594%	0.871%	1.335%	3.740%

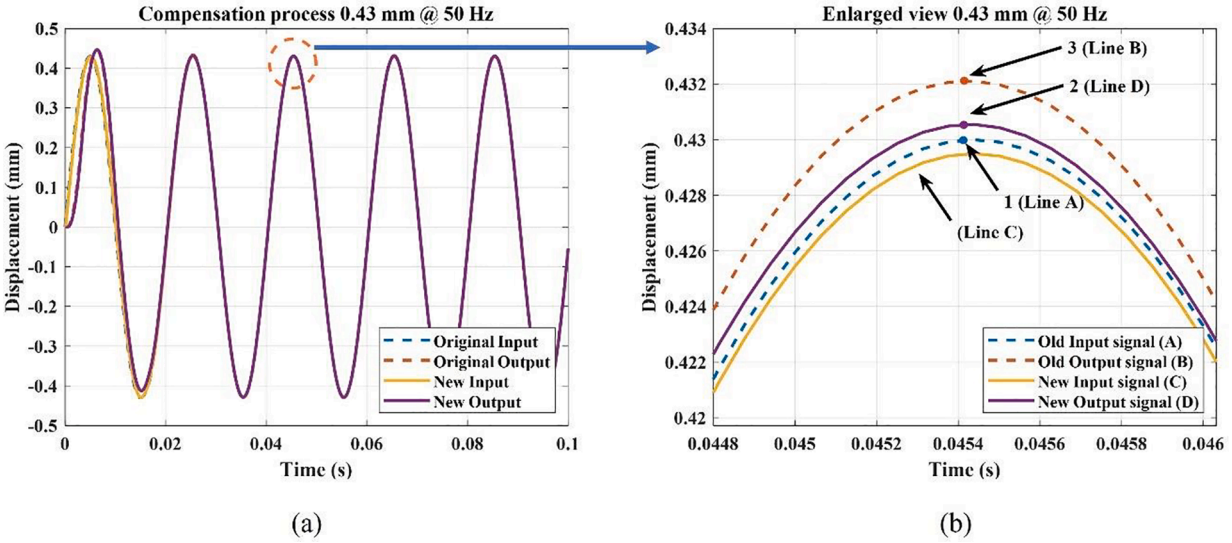

Fig. 10. Compensation process and enlarged view (0.43 mm @ 50 Hz).

$$c(t)_{output} = c(t)_{PID} + c(t)_{SMC} + c(t)_{FF} \tag{5}$$

The control parameters and their functions are listed in Table 1:

The servo frequency is 16 kHz and the output limitation of the controller is ± 10 V. With the designed control algorithm and the open loop identification model, the closed loop simulation model of the system can be built, as shown in Fig. 6. Besides, the tuning process is conducted on the simulation first. The values in Table 1 are achieved when the system simulated tracking error is less than 1%. Same values are used in the physical model to carry on the system performance test.

Table 3
Steady-state error of the designed system after compensation.

Steady-state error (mm & %)				
30 Hz (1 mm)	40 Hz (0.68 mm)	50 Hz (0.43 mm)	60 Hz (0.3 mm)	100 Hz (0.1 mm)
0.00029 0.029%	0.0011492 0.169%	0.0003311 0.077%	0.000249 0.083%	0.000233 0.233%

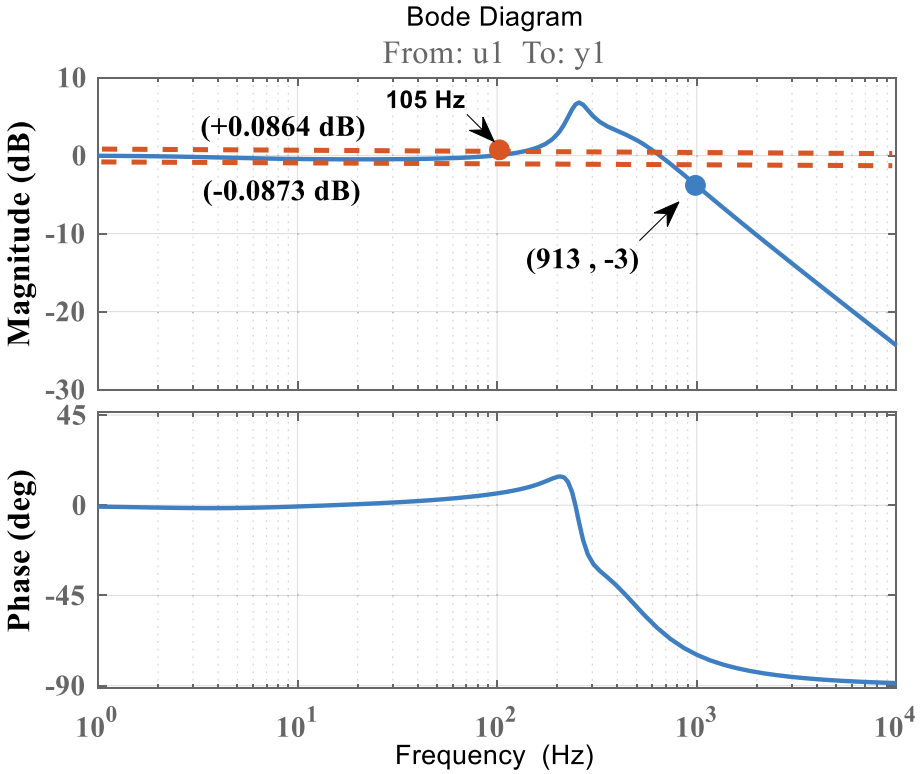

Fig. 11. Bode diagram of the designed FTS system.

3. Performance tests

3.1. Step response and tracking performance tests

Step response and sine wave tracking performance tests were implemented, and the 1 mm step response result is shown in Fig. 7. The rise time is 0.0134 s and zero overshoot is achieved.

In the sine wave tracking performance tests, five different sine signals were generated as input signals: 1 mm @ 30 Hz, 0.68 mm @ 40 Hz, 0.43 mm @ 50 Hz, 0.30 mm @ 60 Hz and 0.10 mm @ 100 Hz. Using 50 Hz and 100 Hz test results as examples, the sine wave tracking performance and tracking error is shown in Figs. 8 and 9 respectively. After the first period, the system reaches steady state (see Fig. 8b). The input and output signals both arrive at the peak point at the same time and no phase errors are observed. The steady-state error is measured as $\pm$ 0.00375 mm, which is 0.871% of the motion amplitude. The tracking error is less than 1%, which indicates that the system achieves good tracking performance. For 100 Hz, after the first two periods, the system reaches steady state (see Fig. 9b). Overshoot and small phase error are observed and the steady-state error is measured at $\pm$ 0.00374 mm, which is 3.74% of the motion amplitude.

The steady-state errors of all testing results are presented in Table 2. The tracking error increases when the working frequency increases. When the system working frequency is close to the maximum bandwidth, it is more difficult to control the system and it maintains good dynamic performance.

A compensation method can be applied to improve the tracking performance further. According to the test results, the input signal amplitudes can be increased or decreased to specific values, and the output signal will then become closer to the command value. The compensation process for 50 Hz is shown in Fig. 10. In the enlarged view, the blue dashed line is the command position signal, and if the input signal is decreased to line C the system output will be line D instead of A. From the maximum displacement points, point 2 is

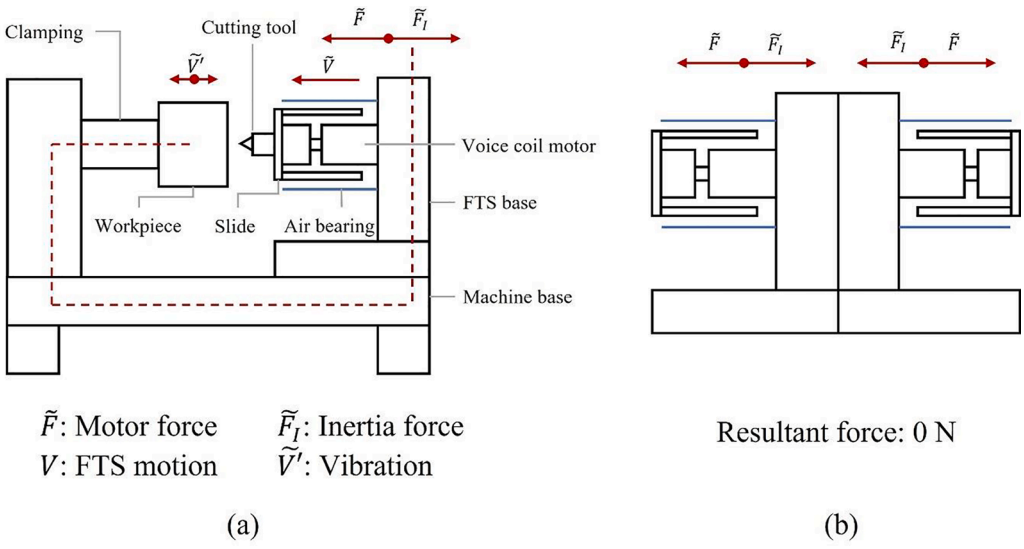

Fig. 12. Sketches of the counterbalance problem and solution.

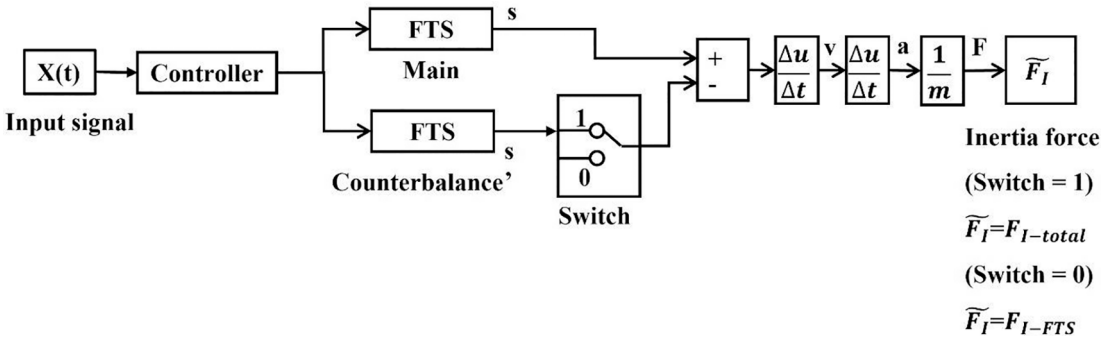

Fig. 13. Control model of the counterbalance.

closer to point 1 than point 3. This means that less overshoot and a smaller tracking error of 0.087% are achieved. The improvements gained using the compensation method are listed in Table 3. The system tracking errors all decrease to less than 1%. The compensation method eliminates the overshoot error at each frequency when no phase error is achieved. In the actual machining, the compensation method can generate a look-up table for the system after the system fine-tuning.

3.2. Bandwidth test

The bandwidth of the system is also a very important index of the system performance. The system closed loop model can be tested by the closed loop frequency sweep and then the Bode diagram of the close loop model can be plotted. The bandwidth can be calculated from the Bode diagram. The closed loop model equation is also described by Eq. (1), but the system order is 5. This means that A is a 5 × 5 matrix, B is a 5 × 1 matrix, C is a 1 × 5 matrix, D is equal to zero and K is a 5 × 1 matrix, which are shown in Eq. (6), The bode diagram of the system is shown in Fig. 11.

$$A=\begin{bmatrix} 0 & 0 & 0 & 0 & 0 \\ -1 & 0 & 0 & 0 & 0 \\ 9.6e^{-6} & 9.6e^{-6} & 1 & -6.3e^{-5} & -0.44 \\ -0.46 & -0.46 & 3.6e^{-7} & 0.998 & 1.4e^{4} \\ -6.6e^{-5} & -6.6e^{-5} & 5.2e^{-11} & -3.7e^{-7} & 0.994 \end{bmatrix},\ B=\begin{bmatrix} 1 \\ 1 \\ 5.3e^{-5} \\ 0.4636 \\ 6.1e^{-5} \end{bmatrix},\ C=[0\quad 0\quad 0\quad 1\quad 0],\ D=0 \tag{6}$$

Normally, the system bandwidth is the frequency when the magnitude is −3 dB, which is 913 Hz for the system. But this means that the output signal decreases to 0.707 of the input signals, which is not suitable for the FTS system, for which higher demand is. Given that the tracking error should be less than 1%, the output signal should remain in the range between 0.99 and 1.01 of the input signal. The range is transformed to dB units from Eq. (7). From the Bode diagram, the system's maximum bandwidth which satisfies the range is 105 Hz. When the system runs at 0–105 Hz, good tracking and dynamic performance can be achieved. Therefore, the designed

Table 4
State-space model parameters of the two FTS systems.

FTS-main		FTS-counterbalance	
A	−11.37	A	−10.243
B	0.0006759	B	0.0008073
C	2.29E+08	C	2.04E+08
D	3.88E−05	D	4.36E−05

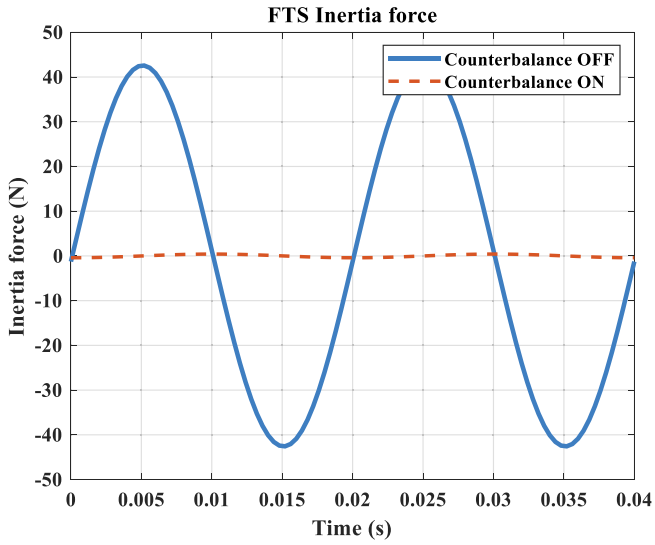

Fig. 14. FTS inertia force (counterbalance ON/OFF).

maximum working frequency is set at 100 Hz. From the bandwidth point of view, the system meets the design requirements:

$$\begin{cases} 20log_{10}0.99 = -0.0873dB \\ 20log_{10}1.01 = +0.0864dB \end{cases} \tag{7}$$

4. Counterbalance

The system motion generates an inertia force that is equal to the motor force. This inertia force can be considered as an external excitation for the whole machining system. This could be transferred from the FTS base through the machine stiffness loop to the workpiece, causing relative dynamic displacements between the cutting tool and workpiece. This process is shown in Fig. 13(a). Normally, the magnitude of this vibration is very small due to the large mass and damping of the machine base, but it is not negligible and significantly affects the machining accuracy in ultra-precision machining. Fig. 12(b) shows a counterbalance solution to this problem by connecting an identical FTS system to the main FTS system. Since two FTSs operate at the same frequency, amplitude and phase angle, then ideally the external excitation becomes the resultant force of two back-to-back connected FTS systems and is cancelled out from the perspective of the machine structure.

It should be noted that the inertia force is equal to the motor force that is related to the system motion. When the counterbalance is working, it does not mean that the whole system is in a state of being stationary. The back-to-back design means that the controller needs to control the two systems simultaneously. The controller works in gantry mode, which synchronizes the two systems as far as possible. However, there are two reasons which could cause the incomplete synchronization of the two systems: a small difference in signal transmission speed between the two encoders; and a difference in internal clock frequency between the two systems. Another cause would be a difference between the two mechanical systems due to manufacturing and assembly errors. Frequency sweeps are carried out for both systems and Eq. (1) is used to describe the FTS-main and FTS-counterbalance. The state-space model parameters are listed in Table 4.

Therefore, considering the FTS control system and characteristics of the counterbalance, the control model of the system with counterbalance can be described as in Fig. 13. For example, with a 0.43 mm @ 50 Hz input signal, the inertia force output of the single FTS system and the counterbalance can be described by Eq. (8) and the total inertia force when the counterbalance is on/off is as shown in Fig. 14.

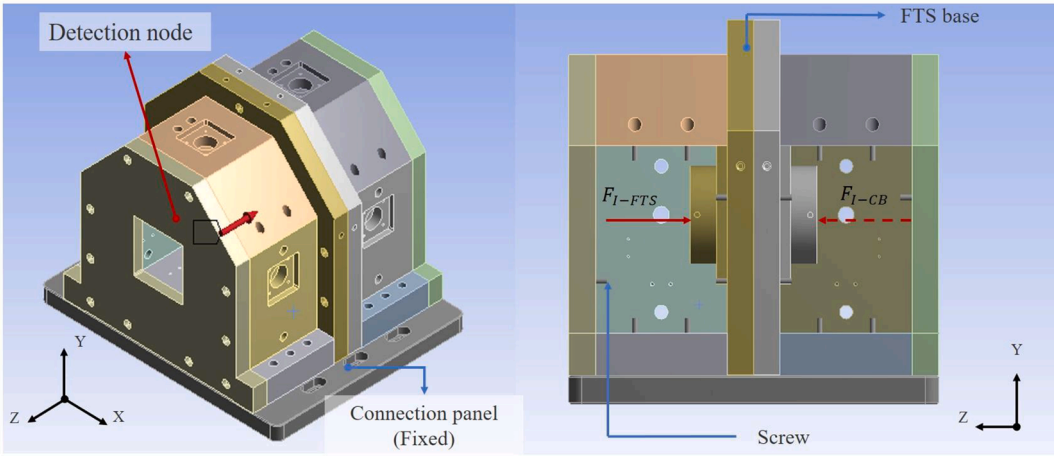

Fig. 15. Simulation model set-up.

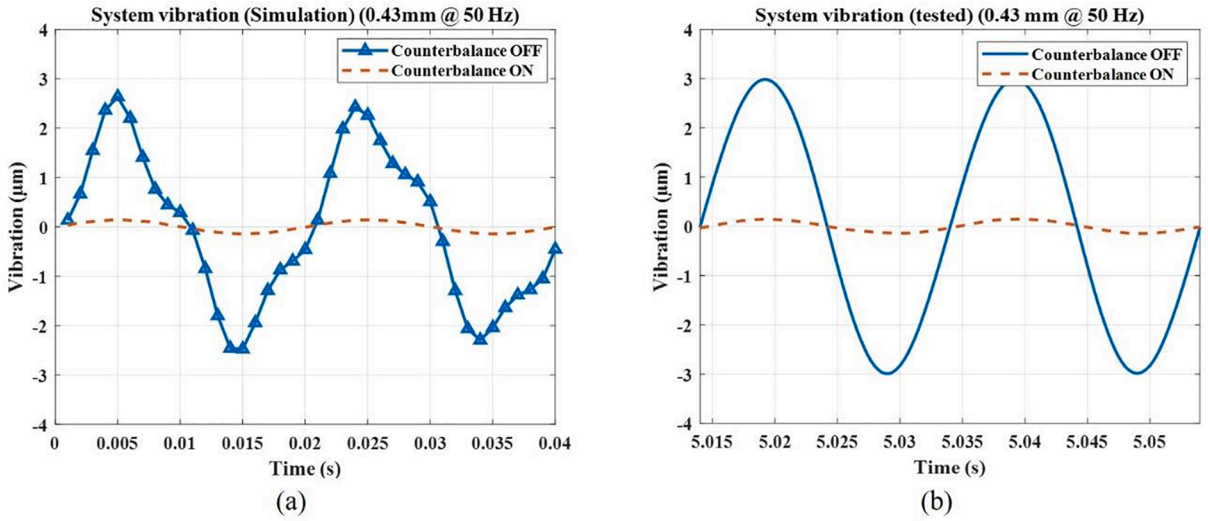

Fig. 16. Comparison of system vibration results.

$$\begin{cases} F_{I-FTS} = 43 \bullet sin(2\pi \bullet 50 \bullet t - 0.02969) \\ F_{I-CB} = 43 \bullet \sin(2\pi \bullet 50 \bullet t - 0.01998) \\ F_{I-total} = F_{I-FTS} - F_{I-CB} \end{cases} \tag{8}$$

where: $F_{I\text{-}FTS}$ is the inertia force of single FTS system (N); $F_{I\text{-}CB}$ is the inertia force of the counterbalance (N); $F_{I\text{-}total}$ is the inertia force of the whole system (N); and t is time (s);

A dynamic simulation model was built in Ansys to simulate system vibration and the effect of the counterbalance on this vibration. When the FTS is working, the inertia force is transferred from the motor coil through the motor magnet and then acts on the FTS base. The base and the connection panel are used to build the solid model, as shown in Fig. 15. The output of the control model (Eq. (8)) is used as a dynamic load input to the simulation model. The deformation in the Z direction of one node (the detection node in Fig. 15) on the front plate is drawn to reflect the system vibration.

In addition to the simulation model, physical tests of the system vibration were performed. A laser displacement sensor (KEYENCE LK-G5000, repeatability: 0.1 μm, resolution: 1 nm) was adopted to measure the vibration of the front plate close to the detection node position in the simulation model. The results of the comparison are shown in Fig. 16.

Both simulation and testing results show that the amplitude of the system vibration is ± 3 μm when the counterbalance is off and the vibration decreases to ± 0.15 μm when the counterbalance is on. Also, the vibration has a sinusoidal motion and shares the same frequency with the system motion. This verifies that the simulation model is accurate and the same frequency with system motion shows that the system vibration is primarily caused by the system motion.

Overall, the back-to-back counterbalance design can effectively suppress the system vibration. When the counterbalance is

Table 5
Cutting and FTS parameters used in the machining experiments.

Tests	FTS Stroke (mm)	FTS Frequency (Hz)	Spindle speed (rpm)	Depth of cut (μm)	Feedrate (mm/min)	Counter-balance
A	1	30	187	10	3	OFF
B	1	30	187	10	3	ON
C	0.5	40	253	10	3	OFF
D	0.5	40	253	10	3	ON

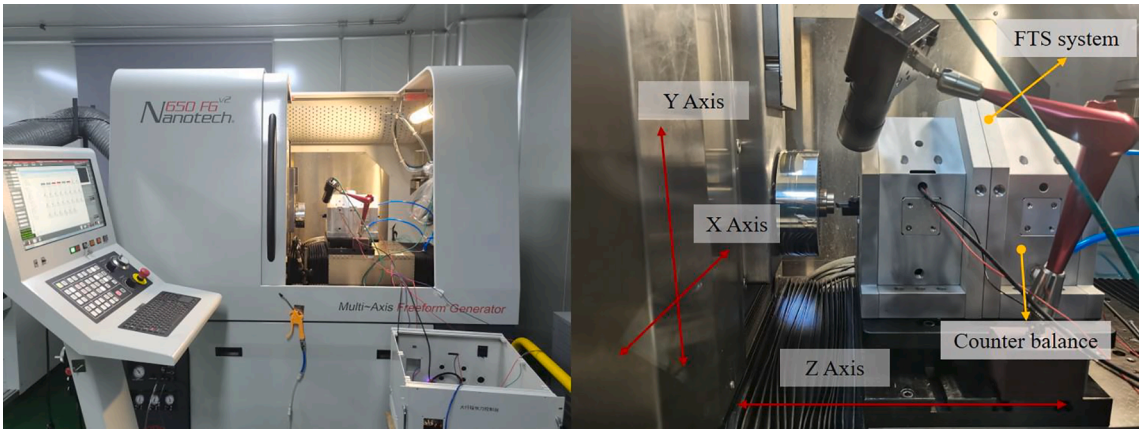

Fig. 17. Experimental settings.

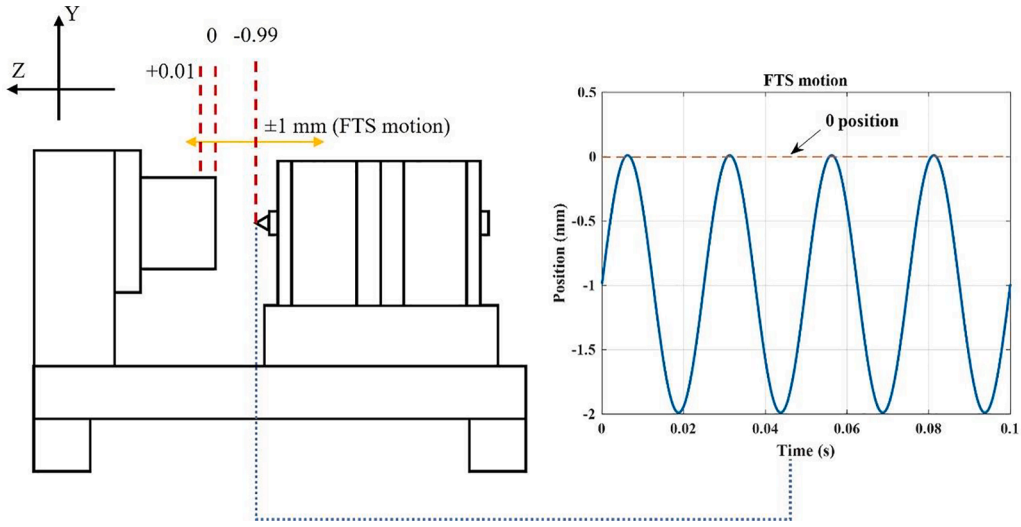

Fig. 18. Tool position settings.

working, the amplitude of the system vibration is decreased to 0.145 μm, which would have very little effect on machining accuracy.

5. Machining experiments

5.1. Experimental design

Machining experiments were designed to test the performance of the FTS system and the efficiency of the counterbalance. The FTS system was installed on the Z axis of an ultra-precision diamond turning machine (Nanotech 650FGv2). Four machining tests were performed and the machining and FTS parameters are listed in Table 5. The FTS strokes were set at 1 mm or 0.5 mm. After the tool setting, the tool position was offset by 0.99 mm or 0.49 mm away from the workpiece surface. These settings can ensure that a depth of cut of 10 μm is achieved at large FTS strokes. The experiment and tool position set-up are shown in Figs. 17 and 18 respectively.

Table 6
Microstructured surface simulation parameters.

Simulation parameters			
f_F	FTS frequency	r_k	Cutting point radius
f_s	Spindle frequency	R_w	Cutting radius
I_f	Nonnegative integer	S_f	Feed rate
D_f	Fractional part	k	Simulation points
$X_{i,j}$	X-coordinate	h	Profile height
$Y_{i,j}$	Y-coordinate	A	FTS stroke
r	Polar radius	d	Cutting depth
θ	Polar angle	R_{dt}	Tool radius

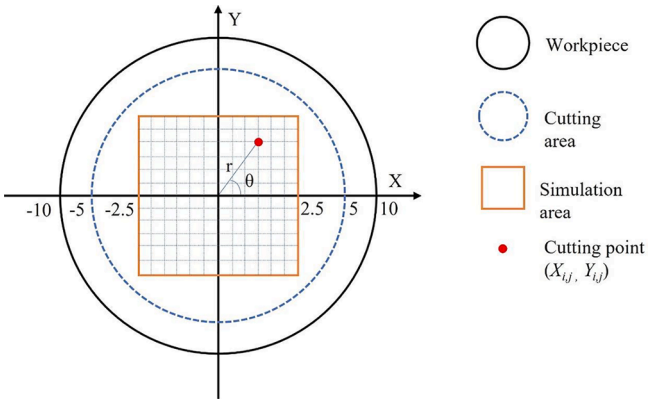

Fig. 19. Schematic of the microstructured surface simulation.

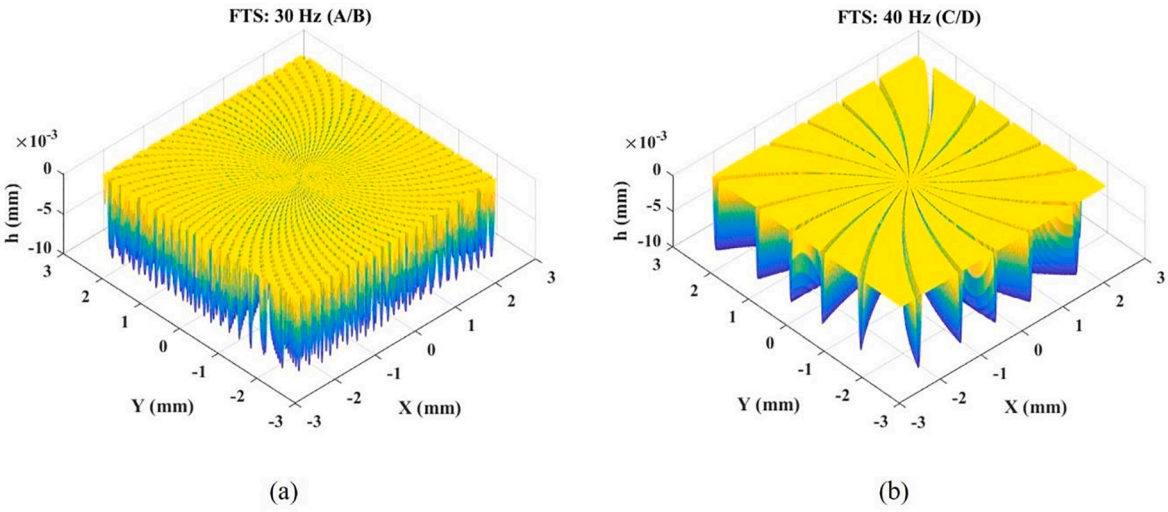

Fig. 20. Simulation of the designed experiments: (a) Tests A and B; (b) Tests C and D.

All experiments used a single crystal diamond tool with a nose radius of 0.25 mm, 0° tool rake angle and 9° tool clearance. The 20 mm diameter copper workpiece was fixed on the spindle through a vacuum chunk. Performance was assessed in three aspects. Firstly, the machine axes following errors from the machine encoders were analysed to determine the effects of the counterbalance on the whole machining system. Then, the motion profile of the FTS during the machining process was analysed. Finally, the machined microstructure surface profile and surface roughness were measured using a 3D optical surface profiler (Zygo Newview 9000). The difference between the depth of the microstructured surface and the target depth was used to assess the accuracy of the FTS motion and surface roughness in determining the efficiency of the counterbalance in the experiments.

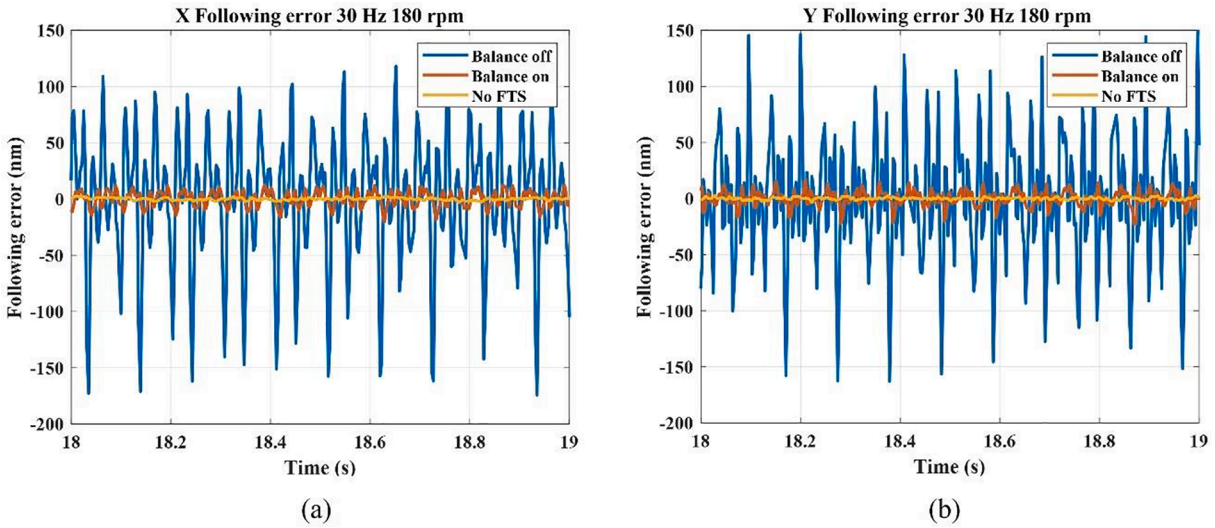

Fig. 21. Following error: (a) X axis; (b) Y axis.

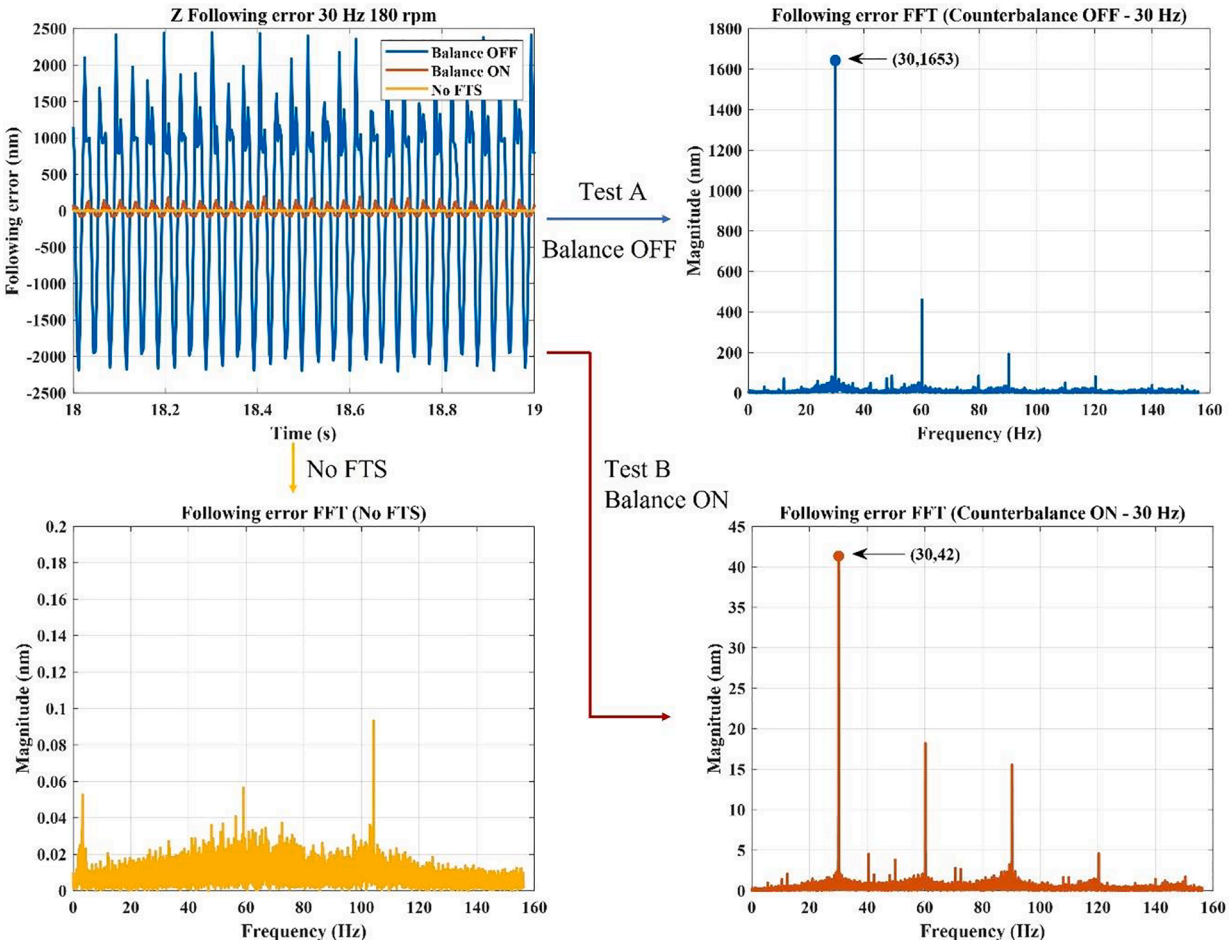

Fig. 22. Z axis following error.

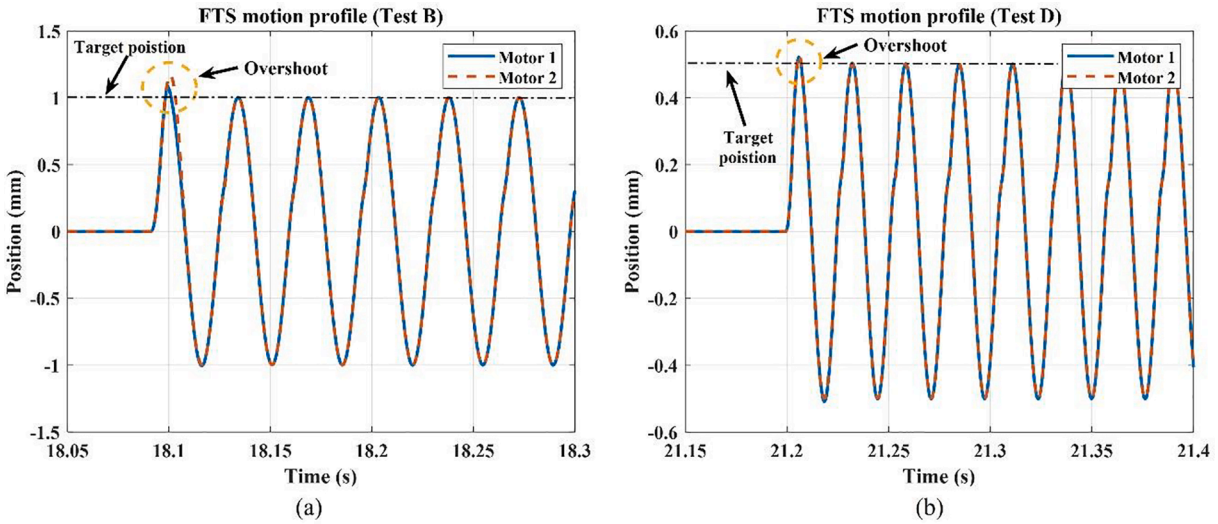

Fig. 23. FTS motion profiles (Tests B and D).

5.2. *Microstructured surface simulation*

A microstructured surface generation model was built to simulate the surface profile before the machining experiments. Considering simple harmonic motion and the tool profile, the simulation model can be built from Eqs. (10) to (13) and Table 6. The simulation range is 5 mm × 5 mm and the resolution is 0.01 mm, as illustrated in Fig. 19.

$$\frac{f_F}{f_S} = I_f + D_f \tag{9}$$

$$\begin{cases} r = \sqrt{X_{i,j} + Y_{i,j}} \\ \theta = arctan(Y_{i,j}/X_{i,j}) \end{cases} \tag{10}$$

$$r_k = R_w - S_f\left(k + \frac{\theta}{2\pi}\right) \tag{11}$$

$$h = A \bullet \{\sin[\mathrm{I_f} \bullet \theta + \mathrm{D_f} \bullet (2\mathrm{k}\pi + \theta)]\} + (\mathrm{A} - \mathrm{d}) + \mathrm{R_{dt}}\left[1 - \sqrt{1 - \left(\frac{\mathrm{r} - \mathrm{r_k}}{\mathrm{R_{dt}}}\right)^2}\right] \tag{12}$$

In the simulation model, the tool path can be generated from the calculation of cutting point position and profile height. The schematic of the microstructured surface simulation is shown in Fig. 19. Besides, the effects of the system vibration on the microstructured surface are not considered, which means that the simulation model simulates an ideal cutting process. The simulation results for the experiments are shown in Fig. 20.

6. Results and discussion

The following errors of the three axes in the turning machine are shown in Figs. 21 and 22. A reference (named 'No FTS') was made by only turning on the spindle without running the FTS system. Tests A, B and the reference are compared to see the effects of the counterbalance. It is clear from the X/Y axis following error that, when the FTS is working, the maximum following error increases from 4 nm to 200–300 nm. This increase means that the FTS system working without counterbalance will cause the vibration in the turning machine and then the cutting tool's absolute position will be affected. When the counterbalance is working, the maximum following error decreased to 28 nm, which means that the counterbalance can decrease the vibration. The Fast Fourier transform (FFT) was applied to the Z axis data, as shown in Fig. 22.

The frequency-domain analysis shows that the dominant frequency is the same as the FTS working frequency (30 Hz). When the counterbalance was working, the magnitude decreased from 1653 nm to 42 nm. Compared to the results when the FTS was off, this proves that the FTS motion caused the increase in the Z axis following error. Since the Z axis is in the same direction as that if the FTS motion, the following error in the Z axis will affect the accuracy of the cutting depth. The same conclusion can be drawn from Tests C and D. The dominant frequency becomes 40 Hz when the FTS working frequency is 40 Hz. Overall, the counterbalance can decrease the following error of the system and make the whole system work in stable conditions. Almost no vibration on the turning machine and accurate tool motion can be achieved.

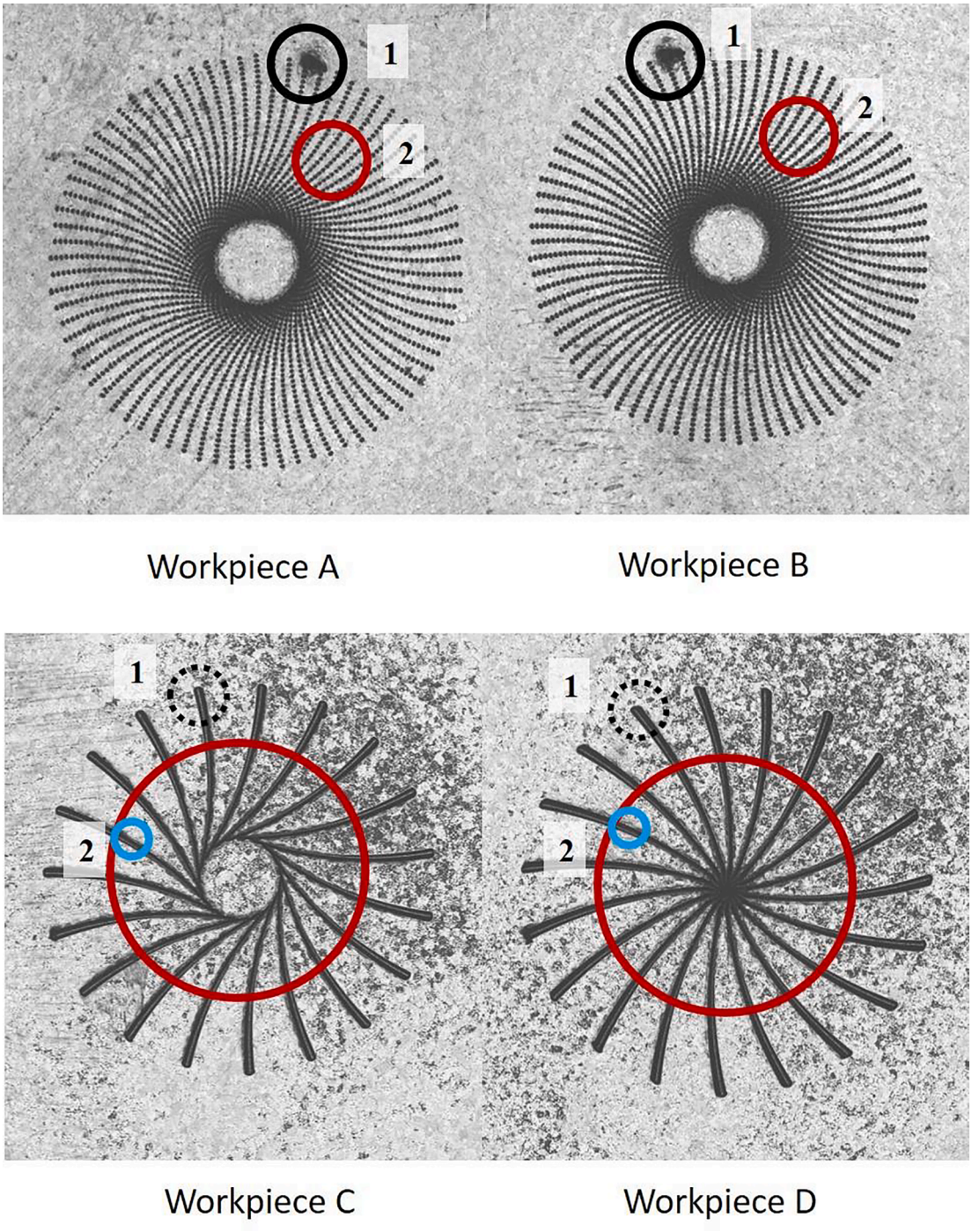

Fig. 24. Topographic characteristics of workpieces.

Next, the FTS motion profile information during machining processes is shown in Fig. 23. Tests B and D are used as examples, 'Motor 1′ is the motor that carries the cutting tool and 'Motor 2′ is the counterbalance motor. The two motors work synchronously in the opposite directions. Fig. 23(a) shows a ± 1.0035 mm stroke and 0.35% tracking error. In the first period, there is an evident 0.0871 mm overshoot, which means at the first cutting point the cutting tool moves 87.1 μm further than expected. Fig. 23(b) shows a ± 0.50339 mm stroke and 0.68% tracking error. The cutting tool moves 21.95 μm further in the first period. The steady tracking error is less than 1%, which meets the design requirements. From the system steady-state performance, the FTS control system has good robustness against cutting resistance. The FTS should start in advance of the real machining processes in order to reach the steady state so as to avoid the overshoot problem. Here, in the experiments, the FTS started at the same time as the machining process and the

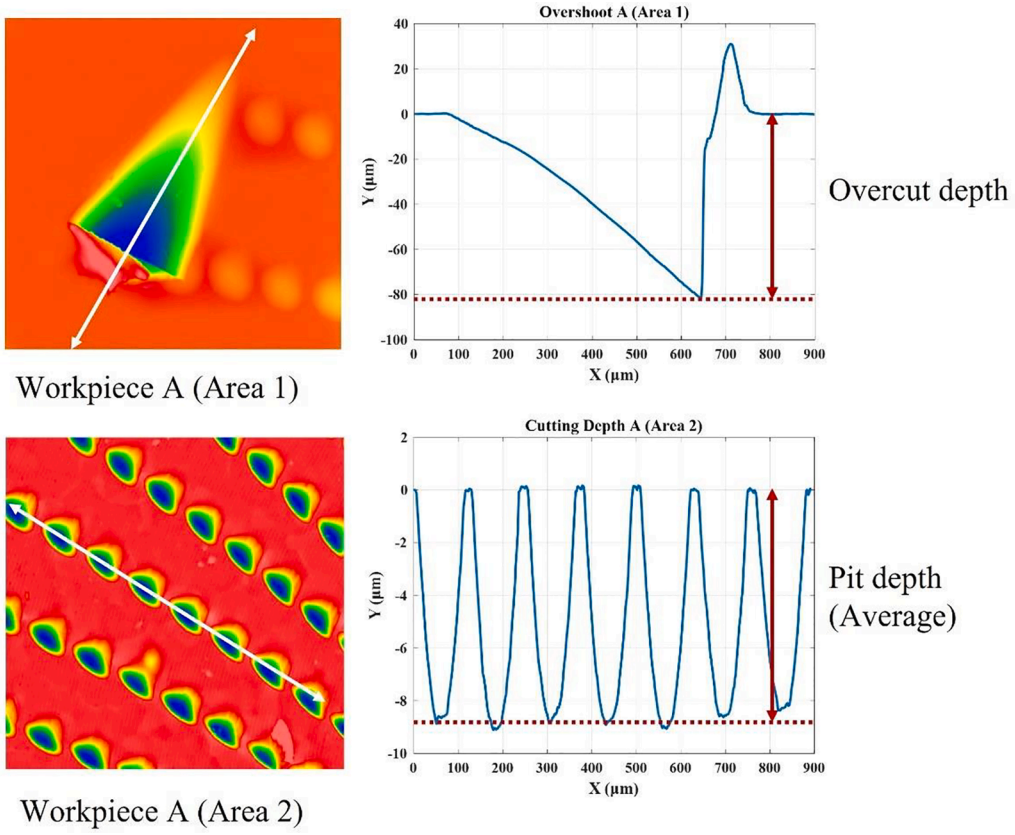

Fig. 25. Enlarged view of A.

overshoot problem remains. The effects of the overshoot on the microstructured surface and its influence on the stability of the FTS system thus can be determined. The microstructured surface was detected by the Zygo optical profiler. From the FTS motion profile, the system can still arrive at a steady state and then reach the required position when the overshoot happens.

Finally, the microstructured surface was measured and the results are shown in Fig. 24. The workpieces A-D correspond to Tests A-D in Table 5. Area 1 in the four workpieces shows the overshoot position which corresponds to the overshoot of the FTS system, while Area 2 corresponds to the stable running condition of the FTS system. The enlarged views and profile data for these two areas are shown in Figs. 25 and 26 (only workpieces A and C are shown). For A and B, the depth of the microstructured surface is the depth of the discontinuous pit. For C and D, the depth of the microstructured surface is the depth of the groove. Note that 19 grooves can be observed from C and D, and the cutting depth is the average of all groove depths. Likewise, for A and B, the cutting depth of the pit is the average value of the pits sampled.

Also, details of the surface roughness of one pit and one groove are shown in Fig. 27. For convenience in interpreting the results, all of the data is shown in Table 7.

The FTS overshoot can be directly reflected in the overcut depth on the microstructured surface. The overcut depth of all four workpieces is close to the FTS overshoot value. The overshoot problem does not affect the system's running condition and the system always goes into steady state and the microstructured surface depths of all workpieces are close to the target depths. The overshoot problem can be avoided by running the FTS system in advance. However, the overshoot problem was deliberately not prevented in these experiments in order to provide a comprehensive analysis of the performance of the FTS. Then, when the counterbalance is off (A and C), the error is more than 10% compared to the target depth of cut of 10 μm. However, when the counterbalance is on, the depth of cut is closer to the target cutting depth. The error is decreased to about 1–2 %. It is noticed that, when the counterbalance is off, the microstructured surface depth is always smaller than the target value. This is because the direction of inertia force is opposite to that of the FTS motion. This force acts on the Z axis of the machine tool and causes the whole FTS system to move along the direction of the inertia force which is against the required motion direction. Finally, in terms of surface roughness, no finishing machining was designed in the experiments, and the surface roughness is at the submicron level. Comparing the surface roughness of workpieces A and B (or C and D), the usage of counterbalance can clearly improve the surface roughness when the cutting parameters are the same. It should be noted that the surface roughness values measured on the FTS machined surface are much higher than those from the diamond turning using large nose radius tools, this is attributed to the large cutting depth and fast tool feed from the FTS used in the experiment. A finishing cut with smaller cutting depth could result in better surface roughness, whereas primary aim of the experiment in this paper is to test the FTS performance.

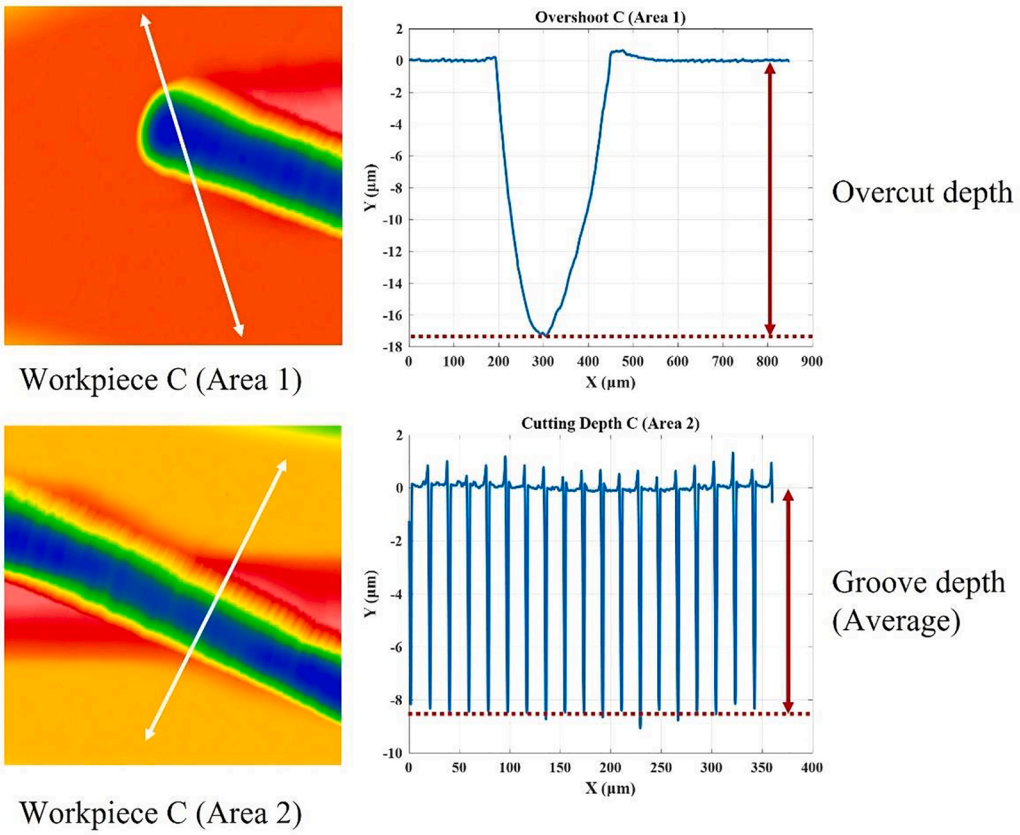

Fig. 26. Enlarged view of C.

In addition, from the microstructured surface, the FTS system's tilt stiffness is not good enough. Cutter relieving happens in Tests A, B and C, where part of the workpiece is not machined (inner circle). This is because the cutting resistance increases instantly when the overshoot occurs and the tool's original position is changed. The tool position's becomes in misalignment from the workpiece rotation centre and the tool motion is changed relative to the workpiece. A sketch of this problem is shown in Fig. 28. This misalignment can be considered to be a drawback of this system.

7. Conclusions and future work

This paper presents a long-stroke fast tool servo system based on voice coil motors and air bearings. Counterbalance is achieved by the back-to-back connection of two identical mechanical subsystems. With a hybrid control algorithm, the system can meet the design requirements with sufficient working bandwidth. Machining experiments were used to assess the FTS system's performance in terms of machining system following errors, the tracking performance of the FTS system's motion, the accuracy of the cutting depth, and the final surface roughness of the workpiece. Specific conclusions are drawn as follows:

The designed fast tool servo system based on a voice coil motor and air bearings can achieve a stroke from $\pm$ 0.1 mm to $\pm$ 1.5 mm with 100 Hz maximum working frequency. The working system bandwidth is 105 Hz and less than 1% tracking error can be achieved with a hybrid control algorithm which combines PID control, sliding mode control and feed-forward control. The system step response and sine wave tracking tests demonstrated that the designed FTS has good tracking performance.

Counterbalance has great benefits to diamond turning processes with an FTS system. Firstly, it can reduce the vibration of the FTS system from $\pm$ 3 μm to $\pm$ 0.145 μm. Secondly, the following errors of the three axes of the turning machine are barely affected by the motion of the FTS when the counterbalance is on. Finally, workpiece quality is improved by adopting the counterbalance during machining processes. The microstructured surface depth error decreased from 10% to 2% and the surface roughness is also reduced.

During machining tests, a first period overshoot occurs in the control system. The FTS overshoot is reflected in the workpiece becoming overcut. After the first period, good robustness can be observed from the steady-state performance of the system.

Declaration of Competing Interest

The authors declare that they have no known competing financial interests or personal relationships that could have appeared to

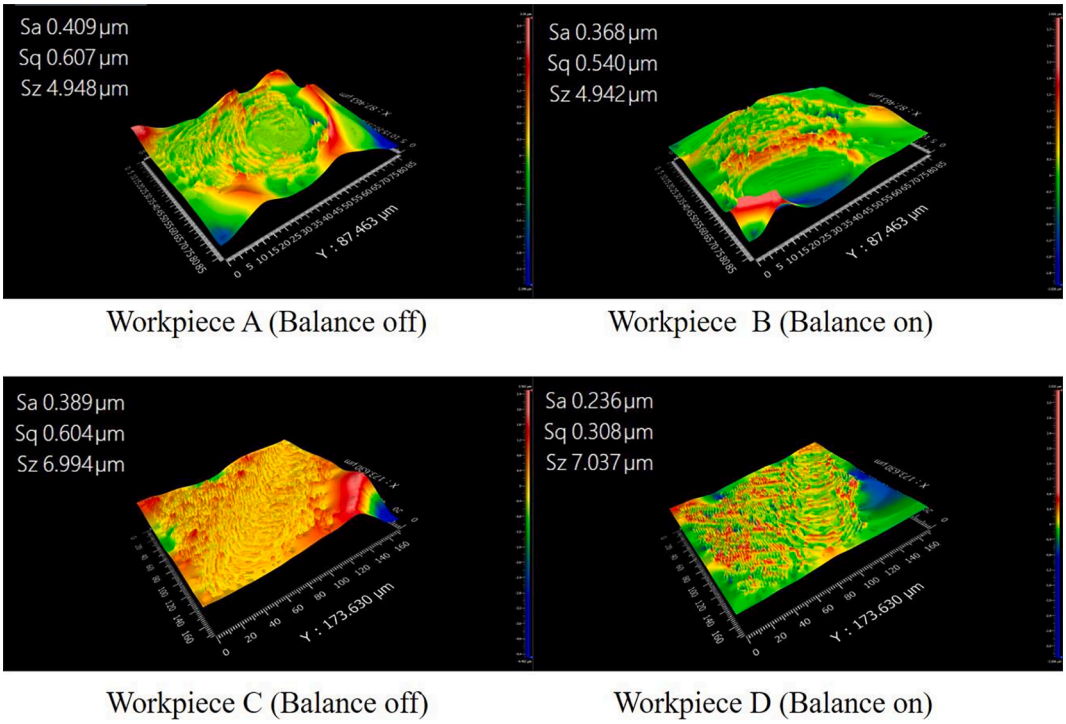

Fig. 27. Surface roughness of workpieces.

Table 7
Target data of designed experiments.

	FTS overshoot (μm)	Overcut (μm)	Depth (μm)	Error	Surface roughness (μm)
A	84.8	81.9224	8.9135	10.865%	0.409
B	87.1	78.0328	10.1406	1.406%	0.368
C	21.95	17.3325	8.4355	15.645%	0.389
D	22.58	18.0803	9.7735	2.265%	0.236

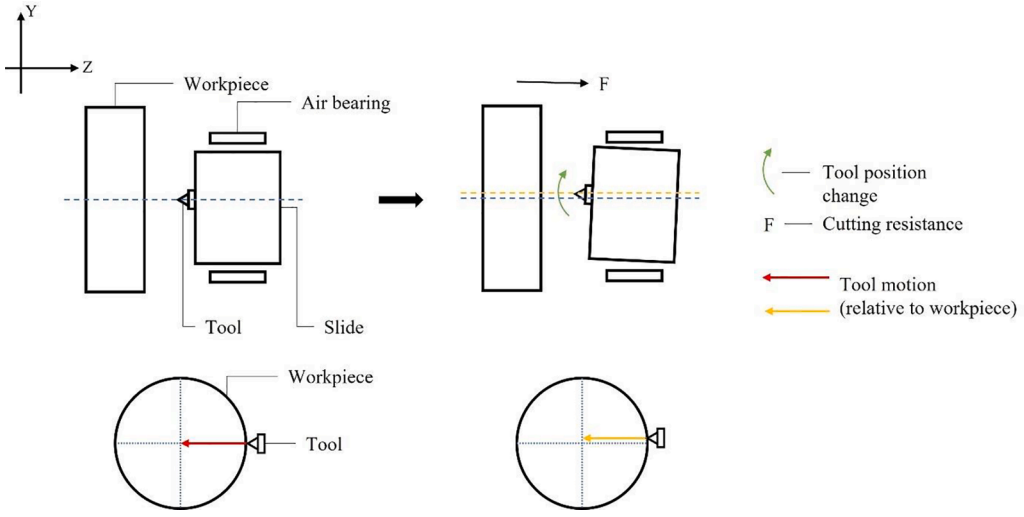

Fig. 28. Sketch of system angle stiffness problem.

influence the work reported in this paper.

References

[1] D.P. Yu, S.W. Gan, Y.S. Wong, M. Rahman, G.S. Hong, Design of a fast tool servo based diamond turning machine for fabricating micro-structured surfaces, Key Eng. Mater. 443 (2010) 669–674.
[2] D. L. Trumper and X. Lu, "Fast Tool Servos: Advances in Precision, Acceleration, and Bandwidth," *Towar. Synth. Micro-/Nano-systems*, pp. 11–19, 2006.
[3] S.W. Gan, M. Rahman, H.S. Lim, Development of a fine tool servo with force monitoring system for nanomachining applications, J. Vac. Sci. Technol. B Microelectron. Nanom. Struct. 27 (3) (2009) 1272.
[4] H. Ma, J. Tian, D. Hu, Development of a fast tool servo in noncircular turning and its control, Mech. Syst. Signal Process. 41 (1–2) (2013) 705–713.
[5] Precitech FTS 70/35, "FTS 70/35 Fast tool servo," *Precitech*, 2021. [Online]. Available: https://www.precitech.com/product/accessoriesoverview/fasttoolservo. [Accessed: 30-Dec-2021].
[6] H. Wang, S. Yang, Design and control of a fast tool servo used in noncircular piston turning process, Mech. Syst. Signal Process. 36 (1) (2013) 87–94.
[7] T. A. Dow, K. Garrard, and A. Sohn, "Fast long range actuator (flora II) for freeform optical surfaces," *Proc. - ASPE Spring Top. Meet. Control Precis. Syst. ASPE 2010*, vol. 48, no. Flora Ii, pp. 96–101, 2010.
[8] M. F. Byl, "Design and Control of a Long Stroke Fast Tool Servo," no. 1993, p. 384, 2005.
[9] H. Feng, et al., Fabrication of freeform progressive addition lenses using a self-developed long stroke fast tool servo, Int. J. Adv. Manuf. Technol. 91 (9–12) (2017) 3799–3806.
[10] Q. Liu, X. Zhou, Z. Liu, C. Lin, L. Ma, Long-stroke fast tool servo and a tool setting method for freeform optics fabrication, Opt. Eng. 53 (9) (2014), 092005.
[11] Precitech, "FTS 5000 Fast tool servo," 2000. [Online]. Available: https://www.precitech.com/-/media/ametekprecitech/documents/brochures/accessories/fast-tool-servo/fts-5000-brochure-180718.pdf?la=en&revision=da87a8b2-1df3-48f5-8586-e21413e98417&hash=91E9BE91A26A0E3052B5A274F7C3125B. [Accessed: 17-Sep-2020].
[12] Z. Wu et al., "High dynamic control of a flexure fast tool servo using on-line sequential extreme learning machine," *IEEE/ASME Int. Conf. Adv. Intell. Mechatronics, AIM*, vol. 2018-July, pp. 604–609, 2018.
[13] X. Zhou, Z. Zhu, S. Zhao, J. Lin, J. Dou, An improved adaptive feedforward cancellation for trajectory tracking of fast tool servo based on fractional calculus, Procedia Eng. 15 (2011) 315–320.
[14] D. Wu, K. Chen, X. Wang, Tracking control and active disturbance rejection with application to noncircular machining, Int. J. Mach. Tools Manuf. 47 (15) (2007) 2207–2217.
[15] H. Zhang, G. Dong, M. Zhou, C. Song, Y. Huang, K. Du, A new variable structure sliding mode control strategy for fts in diamond-cutting microstructured surfaces, Int. J. Adv. Manuf. Technol. 65 (5–8) (2013) 1177–1184.
[16] F. Duan, W.-L. Zhu, A. Sun, B.-F. Ju, Systematic modeling and rapid control for diamond machining of periodical optical surface, J. Manuf. Processes 56 (2020) 451–462.
[17] L. Zhu, Z. Li, F. Fang, S. Huang, X. Zhang, Review on fast tool servo machining of optical freeform surfaces, Int. J. Adv. Manuf. Technol. 95 (5–8) (2018) 2071–2092.
[18] D. Xie, J.Q. Zhu, F. Wang, Fuzzy PID control to feed servo system of CNC machine tool, Procedia Eng. 29 (2012) 2853–2858.
[19] C.Y. Lin, P.Y. Chen, Precision tracking control of a biaxial piezo stage using repetitive control and double-feedforward compensation, Mechatronics 21 (1) (2011) 239–249.
[20] Q. Chen, T. A. Dow, K. Garrard, A. Sohn, and D. Richardson, "Control of a fast long range actuator (FLORA)," *Proc. 23rd Annu. Meet. Am. Soc. Precis. Eng. ASPE 2008 12th ICPE*, pp. 1–4, 2008.
[21] E.M. Zdanowicz, Design of a Fast Long Range Actuator – FLORA II, North Carolina State University, 2009.
[22] M. F. Byl and D. L. Trumper, "A long stroke fast tool servo with integral balance mass," *Proc. 20th Annu. ASPE Meet. ASPE 2005*, 2005.
[23] H. Liu, Y. Sun, B. Zhu, Y. Hu, and W. Xie, "Inertial force control and balance error analysis of fast tool servo based on the voice coil motor," *ICAC 2014 - Proc. 20th Int. Conf. Autom. Comput. Futur. Autom. Comput. Manuf.*, no. September, pp. 243–247, 2014.
[24] Z. Gong, D. Huo, Z. Niu, W. Chen, I. Shyha, Investigation of control algorithm for long-stroke fast tool servo system, Precis. Eng. 75 (2022) 12–23.